Swift monitoring of a Very Faint X-ray Transient Swift J1357.2-0933 during its 2019 outburst

Jahanvi

A dissertation submitted for the partial fulfilment of BS-MS dual degree in Science

Supervisor: Dr. Aru Beri

Indian Institute of Science Education and Research Mohali
April 2020

Certificate of Examination

This is to certify that the dissertation titled **"Swift monitoring of a Very Faint X-ray Transient Swift J1357.2-0933 during its 2019 outburst"** submitted by **Jahanvi** (Reg. No. MS15025) for the partial fulfillment of BS-MS dual degree programme of the Institute, has been examined by the thesis committee duly appointed by the Institute. The committee finds the work done by the candidate satisfactory and recommends that the report be accepted.

Dr. Aru Beri (Supervisor)

Dr. Jasjeet S. Bagla

Dr. K.P. Singh

Dr. Kinjalk Lochan

Dated: April 28, 2020

Declaration

The work presented in this dissertation has been carried out by me under the guidance of Dr. Aru Beri at the Indian Institute of Science Education and Research Mohali.

This work has not been submitted in part or in full for a degree, a diploma, or a fellowship to any other university or institute. Whenever contributions of others are involved, every effort is made to indicate this clearly, with due acknowledgement of collaborative research and discussions. This thesis is a bonafide record of original work done by me and all sources listed within have been detailed in the bibliography.

Jahanvi
(Candidate)

Dated: April 28, 2020

In my capacity as the supervisor of the candidate's project work, I certify that the above statements by the candidate are true to the best of my knowledge.

Dr. Aru Beri
(Supervisor)

Acknowledgment

A successful work of Dissertation is the result of inspiration, support, guidance, motivation and cooperation of facilities during study. It gives me great pleasure to acknowledge my deep sense of gratitude to present my thesis titled: "Swift monitoring observations of a Very Faint X-ray Transient Swift J1357.2-0933 during its 2019 outburst". I am thankful to my respected thesis supervisor Dr. Aru Beri for her whole-hearted support and affectionate encouragement without which my successful thesis would not have been possible. I would like to thank my committee members Dr. Jasjeet Singh Bagla, Dr. K.P. Singh and Dr. Kinjalk lochan for their fruitful advices during committee discussion. I would like to acknowledge NASA's helpdesk regarding my queries for the use of HEASoft FTOOLS. A special thanks to my friends and family members for their moral support and help.

List of Figures

Abstract

This thesis aims to study the 2019 outburst of Swift J1357.2-0933. This was the third outburst detected from a confirmed black hole source, belonging to a class of Very faint X-ray transients. We have proposed, obtained and used the data of this source from the NASA's Swift observatory for our work. These proposed Swift observations were part of the multi-wavelength campaign (Simultaneous Multiwavelength Astronomy Research in Transients NETwork; SmartNet) of this source. We have analyzed the data obtained with X-ray telescope (XRT) and Ultra-Violet/Optical Telescope (UVOT) aboard Swift, with the aim to compare its emission properties with that observed during its previous outbursts in 2011 and 2017.

Our Swift-XRT results showed that 2019 outburst of Swift J1357.2-0933 lasted for about 83 days and during which the maximum X-ray luminosity observed was about 1.62×10^{33} erg s^{-1}. This value of X-ray luminosity indicated that it might be the faintest of two previous outbursts seen in this source or maybe we have missed out the peak of the 2019 outburst. The results obtained after performing X-ray spectroscopy indicated the presence of significant softening during this outburst. We also observed a correlation between X-ray and optical/UV emission. This trend was quite similar to that observed during its previous outbursts.

In future, we wish to investigate this source further in X-rays using data from NICER observatory.

Key Words: X-ray binaries, Black-hole, Transients, Spectral analysis: XRT

Contents

Introduction

Celestial bodies in the universe emit in a wide range of wavelengths, covering the entire electromagnetic spectrum (refer to Figure 1.1). A thin atmospheric layer encloses our planet such that X-rays photons get absorbed by this layer and cannot reach out to the Earth's surface. X-rays were first observed from the sun, and this led people to search for more X-ray sources in the space. With the advancement of technology, many sensitive detectors were developed, which led us to the discovery of many extra-solar X-ray sources in the universe. X-rays are observed from sources like black holes, neutron stars, etc. through different processes, and to detect these photons, we need space-based satellites.

1.1 X-ray astronomy

The development of X-ray astronomy closely linked to the development of the rockets and satellites as they are necessary to put the detectors above the Earth's atmosphere to detect X-ray photons from the Sun and the extra-solar sources. In 1948, the US Naval Research Laboratory (NRL) detected the solar X-rays for the very first time using V2 rockets, which were developed by Germany. After that, scientists used to believe that the Sun is the only potential source of X-rays as it is closest to the Earth. This also led people to believe that no extra-solar X-ray source can be observed as the X-rays from the Sun will be dominant. Despite that, a handful of people were still looking for the X-ray sources outside our solar system. In 1962, the first extra-solar source was detected by American Science and Engineering (AS&E) during their attempt to detect X-ray photons from the lunar surface. The signal was coming from the constellation Scorpius and later the source was named Sco X-1.

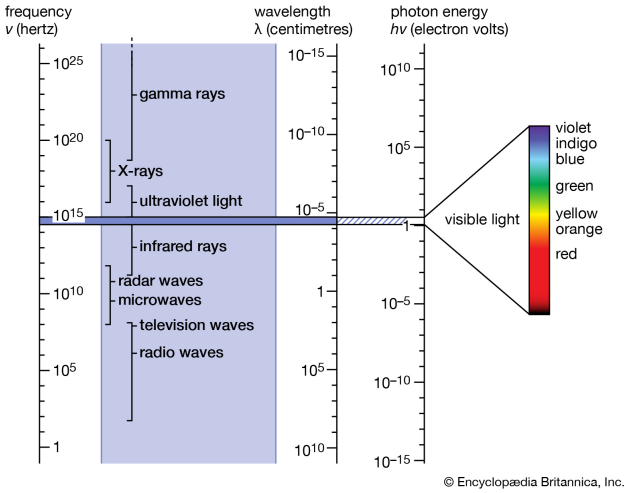

Figure 1.1: Electromagnetic spectrum[1]

After the detection of Sco X-1, the progress in the X-ray astronomy was accelerated. A couple of other X-ray sources were also detected immediately, including the young supernova remnant Crab Nebula. The first extragalactic X-ray source discovered was the active galaxy M87 in 1965. To discover more X-ray sources and understand the underlying processes by which these X-rays are emitted, the first X-ray satellite Uhuru was launched in 1970. Within three years of duration, it discovered a large number of X-ray sources comprising quasars, active galaxies, and cluster of galaxies. Some of the well-known X-ray sources are Cen X-3, Vela X-1, and Her X-1.

Although the Uhuru mission was a success, it did not cover the full sky. The first satellite/observatory designed explicitly for an all-sky survey was HEAO-1, launched in 1979. It detected more than 800 X-ray sources. After a decade, another X-ray satellite, ROSAT, was launched with the purpose of an all-sky survey. It detected nearly 18,000 sources with an order of magnitude better sensitivity than HEAO-1. Currently, more than half-a-dozen of X-ray satellites, including XMM-Newton, Swift, AstroSat, are continuously sweeping the sky to observe different sources and adding to our knowledge about the universe.

1.2 X-ray sources

There are numerous astronomical objects which emit X-rays, for example, galaxy clusters, black-holes in Active Galactic Nuclei (AGN), Gamma-ray bursts (GRBs), supernova remnants, stars, and binary systems containing a compact object (white dwarf, neutron star or

[1]https://www.britannica.com/science/electromagnetic-spectrum

a black-hole) and a star. The Sun is the closest X-ray source to the earth. Not only Sun, but Moon is also an X-ray source as it reflects solar X-rays from its surface. The processes by which these different sources emit the X-ray are entirely different from each other. Hence, one has to deal individually with these various sources. In this thesis, we are focussed towards studying an X-ray binary source: Swift J1357.2-0933. (please see chapter 3 for more details about the source).

1.2.1 X-ray Binaries

X-ray Binaries are the gravitationally bound system consists of a compact object (neutron star or black hole accretes) and a normal star which rotates around a common center of mass. The X-ray emission in these binaries takes place due to the infall of matter onto the compact object from the companion star. Such a mass transfer happens either via the formation of an accretion disk around the compact object, as in the case of Low mass X-ray Binaries (LMXBs) or the stellar wind from the companion star, in case of High mass X-ray Binaries (HMXBs). In all different accretion processes, the fate of the accreted mass depends on the channels by which it loses angular momentum and cools down. The nature of the accretion flow also depends on the type of compact object. For example, if the compact object is a strongly magnetized neutron star, its magnetic field becomes dynamically important close to the stellar surface and determines the properties of the accretion flow. In the case of accreting black holes, the presence of the event horizon (instead of a hard surface and no magnetic field), which does not allow for any stable feature to be anchored to the rotation of the compact object.

1.2.2 Types of X-ray Binaries

X-ray binaries are mainly divided into two different classes, known as high mass X-ray binaries (HMXBs) and low mass X-ray binaries (LMXBs). This classification is based on the mass of the companion stars in the binaries. However, in recent years, astronomers have also discovered binaries with companion's mass intermediate to the companion's mass in LMXBs and HMXBs. These binaries are classified as intermediate-mass X-ray binaries (IMXBs). In this section, we mainly focus on the LMXBs and will briefly discuss the HMXBs and IMXBs.

High mass X-ray binaries (HMXBs)

In HMXBs, the companion is an early type O or B star with mass $8M_{\odot}$ and is more luminous in optical regime than in X-ray regime. The mass transfer in HMXBs takes place via stellar wind. The compact object capture the matter from the powerful stellar wind of the mass-losing star. The observations of these binaries are very helpful in determining the mass and nature of the compact object. The pulsations and eclipses can be observed in HMXBs.

To determine the orbital period, the eclipses in the observed light curve can be measured.

According to the kepler's third law, a binary system will follow the following equation :

$$\frac{(a_x + a_s)^3}{p^2} = \frac{G(M_x + M_s)}{4\pi^2} \tag{1.1}$$

where a_x and a_s are the distances of the compact object and the normal star from the center of mass of the system respectively, $(a_x + a_s)$ is the orbital separation, p is the orbital period, M_x and M_s are masses of the compact object and the normal star respectively. Applying condition that $M_x a_x$=$M_x a_s$, we get

$$Gp^2 \frac{M_s^3 sin^3 i}{(M_x + M_s)^3} = 4\pi^2 a_x^3 sin^3 i \tag{1.2}$$

Since velocity = 2 π radius/orbital period, above formula can be written as the mass function of the binary system [Frank et al., 2002]:

$$f(M) = \frac{M_s^2 sin^3 i}{(M_x + M_s)^2)} = \frac{P_{orb} k^3}{2\pi G} \tag{1.3}$$

where $k = \frac{2\pi a_x sini}{P_{orb}}$ is the velocity of the compact object, and i is the inclination angle, i.e. the angle between the axis of the orbital plane and the line of sight and this factor is included as the observation depends on the inclination angle. The mass of the normal star can be determined by the position in the HR diagram. Equation (1.3) can be used to determine the mass of the compact object.[M.C.Ramadevi,]

Low mass X-ray Binaries (LMXBs)

In LMXBs, the companion star is of low-mass ($\leq 1M_{\odot}$) and evolved to fill its Roche-lobe (instead of having powerful stellar wind like HMXBs) which is equipotential surface and is transferring material through the inner Lagrangian point, L1, onto the compact object. Such mass transfer is more prominent if the donor star is less massive than the Sun, and hence LMXBs will be optically faint, with the donor star usually undetectable. Examples are Sco X-1 and Her X-1.

Fundamental properties and mechanism of mass transfer in LMXBs

These systems are mostly distributed in and around the center of the galaxy as they are associated with the older population II stars in the galactic bulge. The mass donors in these systems are comparable or less massive than the Sun. Their fundamental model was first developed by Cambridge theoreticians Jim Pringle and Martin Rees in the early 1970s.
The mechanism of mass transfer in LMXBs is totally different than in HMXBs. A slightly evolved late-type star fills its Roche-lobe and transfers material through its inner Lagrangian point onto the compact object, which is either a white dwarf, neutron star or black hole. Because of the angular momentum of the material, as it leaves the star, it cannot fall directly onto the compact object but instead go into orbit around it, thereby forming an accretion disc. [Seward and Charles, 2010]

There is one small group of LMXBs that accrete from the donor wind of the low-mass red giant donor. These systems are known as Symbiotic X-ray binaries. LMXBs with exceptionally short periods and hydrogen deficient donors are often referred as a different class of Ultra-Compact X-ray Binaries (UCXBs).

Properties

- **Eclipse**
  As the compact object and the normal star orbit around their common centre of mass, the normal star hides the compact object once in every orbital period, which obscured the X-rays from the compact object. This can observed as a decrease in the intensity of the X-ray emission. Depending upon the disk geometry and inclination angle, eclipses can be either total or partial. The observations of the eclipses are beneficial in determining the orbital period of the binary system.[M.C.Ramadevi,]

- **X-ray dips**
  When the accretion stream strikes the accretion disk, the X-rays are temporarily obscured by this stream and cause X-ray dips (as shown in Figure 1.2). The impact region where this stream strikes the disk is higher than that of the other parts of the disk. X-ray dips are common in LMXBs and are seen either prior to the eclipse or just after the eclipse. For exmaple, EXO 0748-676 is one of the few LMXBs that show a full eclipse (Figure 1.3). [M.C.Ramadevi,]

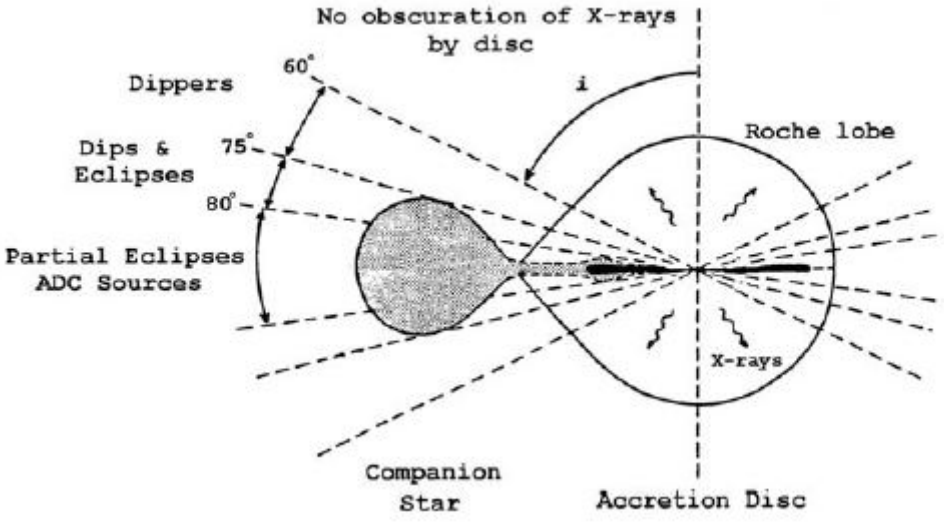

Figure 1.2: Schematic showing eclipses and dips in LMXBs at different inclination [Seward and Charles, 2010]

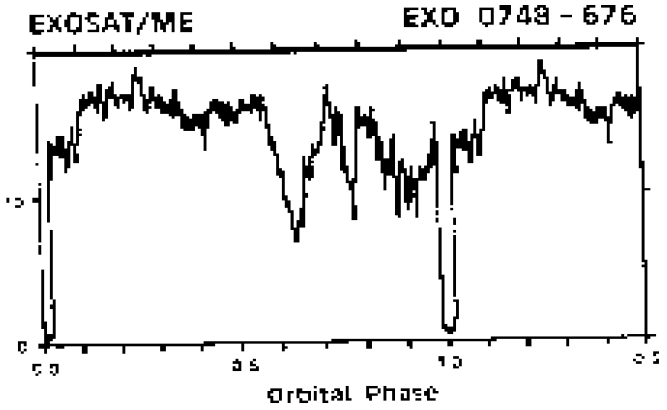

Figure 1.3: Observation of X-ray dips and eclipses in EXO 0748-676 [Seward and Charles, 2010]

- **X-ray bursts**

  In X-ray bursts, the intensity of the X-ray emission increase sharply with a short rise time of about few seconds and a longer decay time. In case of neutron star binaries, this increase in the intensity of the X-ray emission is due to the unstable nuclear burning on the surface of the neutron star. In LMXBs, X-ray bursts can be explained by the Thermonuclear flash model, which is as follows : [Seward and Charles, 2010]

  - The accreted matter onto the surface of the neutron star contains mostly hydrogen. This matter produce a surface layer of hydrogen which burn steadily and produce an underlying layer of helium, which starts burning afterwards.
  - When the helium burning is unstable, all the helium will be burnt rapidly and produce thermonuclear flash that we observe as an X-ray burst.
  - This process repeats again producing further X-ray bursts.

  The radius of the neutron star can be determined by the observations of X-ray bursts if the distance of the source is known. The X-ray emission during a burst is believed to emit as a blackbody radiation. If F_x is the observed flux, d is the distance of the source, R is the radius of the neutron star and T is the temperature at the surface of the neutron star, then one can use the Stefan's law

  $$4\pi d^2 F_x = 4\pi R^2 \sigma T^4 \tag{1.4}$$

  Rearranging the above terms, we will get

  $$R = (d/T^2)(F_x/\sigma)^{0.5} \tag{1.5}$$

  The values of F_x and T are obtained from the observation.
  Since this whole process takes place on the surface layers of a neutron star, the observation of the X-ray bursts from an X-ray source rules out the possibility of the compact object being a black hole.[M.C.Ramadevi,]

- **Quasi-periodic oscillations**

  The Quasi-periodic oscillations (QPOs) are the characteristics of LMXBs. In QPOs, the intensity of X-rays produced vary quasi-periodically. This variability in X-rays

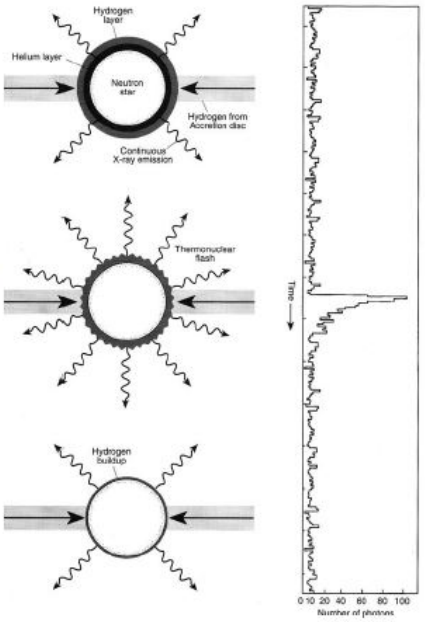

Figure 1.4: Schematic representation of Thermonuclear flash model for an X-ray burst (figure taken from [Seward and Charles, 2010]

can be well explained by the beat-frequency model which is as follows: The inner part of the accretion disc is in close contact with the neutron star. The neutron star rotates with a particular frequency and the matter surrounding it rotates around it with an orbital frequency. The difference between the spin frequency of the neutron star and the orbital frequency of the inner disc is known as the Beat frequency.[M.C.Ramadevi,]

Figure 1.5 tabulated the observed properties of HMXBs and LMXBs.

Intermediate mass X-ray Binaries (IMXBs)

Intermediate mass X-ray binaries (IMXBs) are systems consist of a compact object (a neutron star or a black-hole), and an intermediate-mass star with a mass roughly lies between $1.5M_{\odot} - 10M_{\odot}$. Here the companion star is A or F type. Although IMXBs are known as the origin of Low mass X-ray binaries (LMXBs), we know very little about them (see [Shao and Li, 2015] for more details). In IMXBs, the mass of the companion star is not high enough to produce sufficiently high wind mass-loss rates to power an observable X-ray source. The mass transfer in IMXBs mostly occurs through Roche-lobe Overflow. When an IMXB evolves through Roche-lobe overflow, the relatively large mass ratio between the companion star and the neutron star causes this phase to be short-lived ($\sim 1000\,yr$) with a

	HMXB	LMXB
X-ray spectra:	$kT \geq 15$ keV (hard)	$kT \leq 10$ keV (soft)
Type of time variability:	regular X-ray pulsations no X-ray bursts	only a very few pulsars often X-ray bursts
Accretion process:	wind (or atmos. RLO)	Roche-lobe overflow
Timescale of accretion:	10^5 yr	$10^7 - 10^9$ yr
Accreting compact star:	high $\vec{B}$-field NS (or BH)	low $\vec{B}$-field NS (or BH)
Spatial distribution:	Galactic plane	Galactic center and spread around the plane
Stellar population:	young, age $< 10^7$ yr	old, age $> 10^9$ yr
Companion stars:	luminous, $L_{\rm opt}/L_x > 1$ early-type O(B)-stars $> 10\,M_\odot$ (Pop. I)	faint, $L_{\rm opt}/L_x \ll 0.1$ blue optical counterparts $\leq 1\,M_\odot$ (Pop. I and II)

Figure 1.5: Observed properties of galactic X-ray sources (table taken from [Tauris and van den Heuvel, 2003]).

very high mass transfer rate $\sim 10^{-4} M_\odot yr^{-1}$. Her X-1 and GRO J1655-40 belong to this class.

1.2.3 The power of accretion

High energy radiation in X-ray binaries, AGNs, quasars, etc. are produced by a powerful mechanism known as accretion. The gravitational potential energy released by an accretion of a body of mass m on the surface of body of mass M and radius $R_\star$ is given by

$$\Delta E_{acc} = \frac{GMm}{R_\star} \tag{1.6}$$

Thus, it is evident from the above equation that the efficiency of accretion is strongly dependent on the compactness of the accreting object. More compact the object, the more energy will release. The rate of the accreting mass is related to the luminosity resulting from the accretion. This relation is given by

$$L = \frac{GM(dM/dt)}{R} \tag{1.7}$$

where R and M are the radius and the mass of the compact object, and dM/dt is the rate of the matter accretion. Above expression can be rewrite as :

$$L = \eta \frac{dM}{dt} c^2 \tag{1.8}$$

where $\eta = \frac{GM}{Rc^2}$ is the efficiency.[M.C.Ramadevi,]

1.2.4 The Eddington limit

The electromagnetic radiation produced during the accretion exerts pressure on the material. This pressure is proportional to the flux of the radiation. The luminosity at which the radiation pressure overcome the gravitational potential of the compact object ceases the accretion of matter. This luminosity is known as the Eddington luminosity, given by

$$L_E = \frac{4\pi GMm_pc}{\sigma_\circ} \tag{1.9}$$

where $\sigma_\circ$ is the Thomson scattering cross-section, M is the mass of the compact object, m_p is the mass of the proton, c is the velocity of light. Substituting the values of the constants in the above equation, we get

$$L_E = 1.3 \times 10^{38}(\frac{M}{M_\odot})erg/s \tag{1.10}$$

1.2.5 Accretion processes in the X-ray binary systems

There are two main types of accretion processes that are relevant to X-ray binary systems, namely: Roche-lobe overflow and Stellar wind.[M.C.Ramadevi,]

Roche-lobe overflow

The gist of the Roche-lobe problem is to consider the orbit of a test particle in the gravitational potential due to two massive bodies orbiting each other. These are so massive that the test particle does not affect their orbits. Thus, these two bodies execute Kepler orbit about each other in a plane: the Roche problem assumes these orbits to be circular. Besides this, it is also assumed that the two stars are 'centrally condensed' in the sense that they can be regarded as point masses. Let the masses of the two stars are $m_1M_\odot$ and $m_2M_\odot$ where m_1 and m_2 lie in the range of $0.1 - 100$ for all types of stars. The Kepler's third law relates the binary separation, a, and the binary period, P as :[Frank et al., 2002]

$$4\pi^2a^3 = GMP^2 \tag{1.11}$$

where $M = M_1 + M_2 = mM_\odot$. In the alternative forms, 'a' can be expressed as:

$$\begin{pmatrix} 1.5 \times 10^{13} m_1^{1/3} (1+q)^{1/3} P_{yr}^{2/3} cm, \\ 2.9 \times 10^{11} m_1^{1/3} (1+q)^{1/3} P_{day}^{2/3} cm, \\ 3.5 \times 10^{10} m_1^{1/3} (1+q)^{1/3} P_{hr}^{2/3} cm, \end{pmatrix}$$

and mass ratio

$$q = \frac{M_2}{M_1} \tag{1.12}$$

The gas flow between the two stars is governed by the Euler equation which is given as :

$$\rho \frac{\partial \boldsymbol{v}}{\partial t} + \rho \boldsymbol{v} \dot{\nabla} \boldsymbol{v} = -\nabla P + \mathbf{f} \tag{1.13}$$

where $\mathbf{f}$ is the force per unit volume. For simplicity, we can write the above equation (1.13), in a frame of reference rotating with the binary system, with angular velocity ω relative to an inertial frame. Since in this frame, the two stars are fixed which introduces additional terms in the Euler equation because of centrifugal and Coriolis forces. With assumptions made for the Roche problem, the Euler equation can be written as:

$$\frac{\partial \boldsymbol{v}}{\partial t} + (\boldsymbol{v}.\nabla)\boldsymbol{v} = -\nabla \phi_R - 2\omega \Lambda \boldsymbol{v} - \frac{1}{\rho} \nabla P \tag{1.14}$$

where $-2\omega\Lambda v$ is the Coriolis force per unit mass, and $-\Delta\phi_R$ includes the effects of both gravitational and centrifugal force. ω is the angular velocity of the binary, which can be expressed as given below:

$$\boldsymbol{\omega} = \left[\frac{GM}{a^3} \right]^{1/2} \mathbf{e} \tag{1.15}$$

where $\mathbf{e}$ is a unit vector normal to the orbital plane.

Here, ϕ_R is the Roche potential which is given by:

$$\phi = -\frac{GM_1}{|r - r_1|} - \frac{GM_2}{|r - r_2|} - \frac{(\omega \Lambda r)^2}{2} \tag{1.16}$$

where r_1 and r_2 are the distances to the center of the stars or bodies with mass M_1 and M_2, respectively.

Suppose that the orbit is circular due to the tidal forces, and the two components of the binary are co-rotating. In this case, we can define fixed equipotential surfaces in a comoving frame. The Roche-lobe is the equipotential surface passing through the inner

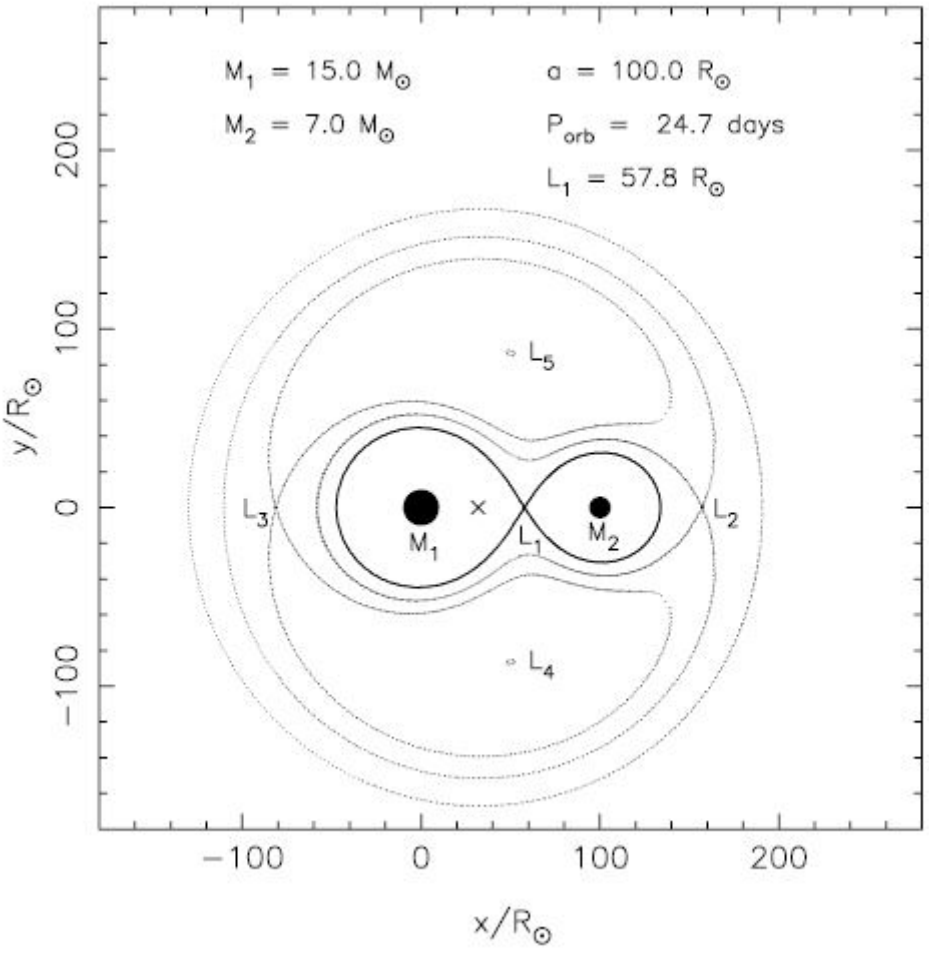

Figure 1.6: A cross-section in the equatorial plane of the critical equipotential surfaces in a binary. The thick curve crossing through L_1 is the Roche-lobe (taken from [Tauris and van den Heuvel, 2003]).

Lagrangian point L_1. If the donor star evolves to fill its Roche-lobe, the pressure at L_1 will be unbalanced and initiate a mass transfer (Roche-lobe overflow) onto the accretor or the compact object. The radius of the donor's Roche-lobe, R_L is given as [Eggleton, 1983]

$$\frac{R_L}{a} = \frac{0.49q^{\frac{2}{3}}}{0.6q^{\frac{2}{3}} + ln(1+q^{\frac{1}{3}})} \tag{1.17}$$

where a is the orbital separation and $q \equiv M_{donor}/M_{accretor}$ is the mass ratio of the binary components.

The shape of the equipotentials depends on q and a. The system appears as a point mass concentrated at the center of mass (CM) to the matter orbiting at large distances $(r >> a)$ from it. Thus, the equipotentials at large distances are just those of a point mass seen in a rotating frame. There are circular equipotential sections around the centers of both stars (r_1, r_2); the motion of matter here is dominated by the gravitational pull of the nearer star. Thus, the potential ϕ_R has two deep valleys on the center of r_1 and r_2. Figure 1.6 is known as figure-of-eight, and it shows how these two valleys are connected. In three-dimensions, this surface will look like a dumbbell shape, and the part surrounding each star is called its Roche-lobe. The lobes meet at the inner Lagrangian point L_1, which is a saddle point of ϕ_R. The material inside any one of the lobes near L_1 finds it much easier to pass through L_1 into the other lobe than to escape the "dumbbell" surface altogether. Suppose, initially, both stars are significantly smaller than their Roche lobes, and the rotation of each star on its axis is synchronous with the orbital motion, with axes orthogonal to the binary plane. Synchronism is generally a safe assumption, as tidal forces tend to bring it about on a timescale similar to that for circularization of the binary orbit. In this case, the surface of each star will agree to one of the approximately circular equipotentials in Figure 1.6. This follows from the Euler equation (1.14) since $v = 0$, and P is constant on the surface. In this case, the material cannot be pulled off either of the stars by the gravitational attraction of the other, and the binary is known as detached. Here, the mass transfer could take place only via the wind mechanism. Suppose, for some reason (e.g., stellar evolution), one of the stars swells up so that its surface, which must lie on an equipotential on ϕ_R, eventually fills its Roche lobe. So, we label the star as star 2, which fills the Roche lobe, and is referred to as a secondary star. A part of the envelope of the secondary star lies very close to the inner Lagrangian point L_1. Any perturbation of this material will push it over the L_1 point into the Roche lobe of the primary star, where it must, eventually, be captured by the primary star (labelled as star 1). Such perturbations are always present, provided, for example, by pressure forces. This system is known as semi-detached, and can efficiently transfer mass

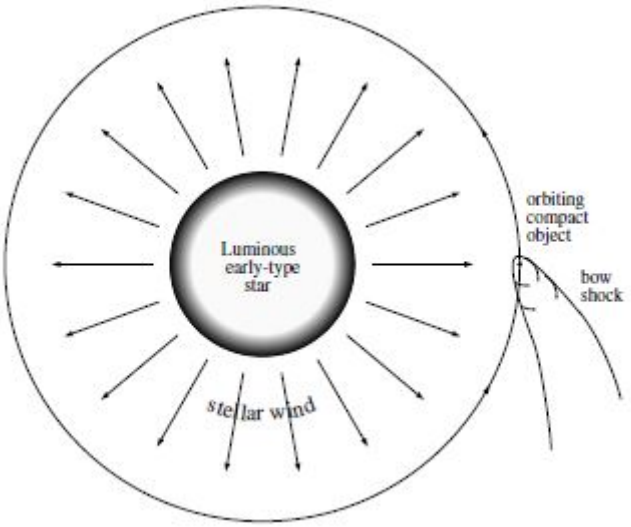

Figure 1.7: Schematic of mass loss via stellar wind in HMXBs [Frank et al., 2002]

from the secondary to the primary for as long as the secondary remains in contact with its Roche lobe. This kind of mass transfer is known as Roche lobe overflow. Since mass is removed from the star immediately once the lobe is filled, the star cannot be significantly larger than its Roche lobe [Frank et al., 2002].

Stellar wind

The mass accretion from the stellar wind is particularly relevant for systems consisting of an early-type (O or B) star and a compact object (a neutron star or a black hole) in a close orbit. The stellar wind of the early-type companion is both powerful, with mass-loss rates $10^{-6} - 10^{-5} M_{\odot} yr^{-1}$, and highly supersonic, with velocity given by,

$$v_w(r) \sim v_{esc}(R_E) = \left(\frac{2GM_E}{R_E}\right)^{1/2}, \tag{1.18}$$

where r is the distance from the center of the early-type star. M_E is the mass and R_E is the radius of the early-type star, and v_{esc} is the escape velocity at its surface.

The compact object captures the mass of the stellar companion from the stellar wind. In high mass X-ray binaries (HMXBs), stellar wind is predominant mass-accretion process. The two main parameters that can be estimated by observing a binary system are mass accretion rate $\dot{M}$, which is the mass loss per unit time by the companion star, and terminal velocity v_c, which is the velocity of the stellar wind at larger distances from the star. These parameters are important because:

- To study the evolution of the stars, $\dot{M}$ is a crucial parameter as low mass stars evolve differently than the high mass stars.
- Many different stellar mass theories predict different mass-loss rates and terminal velocities for a star. So by comparing the observations and predicted values, one can learn the mechanism of mass loss from a star.
- The gas from the star carries kinetic energy with it. The kinetic energy deposits by this gas in the interstellar medium per unit time is $0.5\dot{M}v_c^2$. So to learn the effect of stellar wind on its surrounding interstellar medium, the values of $\dot{M}$ and v_c^2 of the star are required.

The wind velocity varies with the radial distance from the star as per the velocity law, $v(r)$. The velocity law can be approximated by a β-law, which is given by

$$v(r) \simeq v_0 + (v_x - v_0)(1 - \frac{R_.}{r})^{\beta}) \tag{1.19}$$

This law implies that v increases with the distance, i.e., from the photosphere ($r = R_.$) to larger distances. Here β is a variable that defines how 'steep' the velocity law is. The hot stars experience faster acceleration in the wind in comparison to cold stars as β values for cold stars are larger.[Frank et al., 2002]

1.3 X-ray detectors

X-ray detectors are instruments used to detect X-ray signals from cosmic bodies. They are designed to be sensitive so that they can detect photons from far away sources. They contain an electronic circuit that amplifies the received signal and records the time and amplitude of the event. These detectors are designed/structured in such a way that they remain unaffected by vacuum, heat, and cold conditions in space. Detectors are characteristed based on how sensitive it is to the incoming photons, how much resolution does it have, how much sky area it can cover (field of view), and what is its dead-time, i.e., the time when it will not detect the next incoming photon. Some basic properties of X-ray detectors are :

- Quantum Efficiency : It is the ratio of the detected photons to the incoming photons.
- Spectral Range : It is the wavelength range over which the detector is sensitive to the incoming photons.

- Dynamic Range : It is the ratio of the brightest detectable signal to the faintest one.
- Time resolution : It is the time response of any detector. It is the minimum time interval over which change in photons can be detected. It is also known as the readout time.
- Linearity : It means that for every incident photon incident on a detector, an electron should be generated. The more linear a detector is, the more quantum efficiency it will have.

There are many types of X-ray detectors developed until now. We will be briefly discussing these below [arn, 2011].

1.3.1 Proportional Counter

It is one of the X-ray detectors which is used to measure the energy of each incident photon. They collect large number of photons and have a high time resolution of the order of microseconds that allow us to perform fast timing studies to understand the rapid variability in several accretion powered sources. It generally consists of thin windows to transmit a sufficient amount of X-rays, which should be strong enough to withstand the gas pressure inside the detector and do not let it leak. Typically, this window is either made from 0.1 mm Be or even thinner plastic, such as Formvar. Proportional Counters generally contain noble gas. The atoms of this gas absorb the X-ray photon incident on it and produce photoelectrons. These electrons drift towards anode wire, which is maintained at high voltage, and ionize further gas atoms as they collide with it, causing an avalanche of electrons near the anode wire (Figure 1.8). This avalanche amplifies the original signal in a linear way. The detector output sort out the events by size, which form a pulse-height spectrum which is related to the energy of the incident X-rays (through the photoelectrons). All pulses below a certain threshold are rejected to eliminate events from UV photons. Proportional counters were used in many successful X-ray missions, for example, the payload of Uhuru satellite consisted of two sets of proportional counters, and ROSAT consisted of two Position sensitive Proportional counter (PSPC).[Seward and Charles, 2010][arn, 2011]

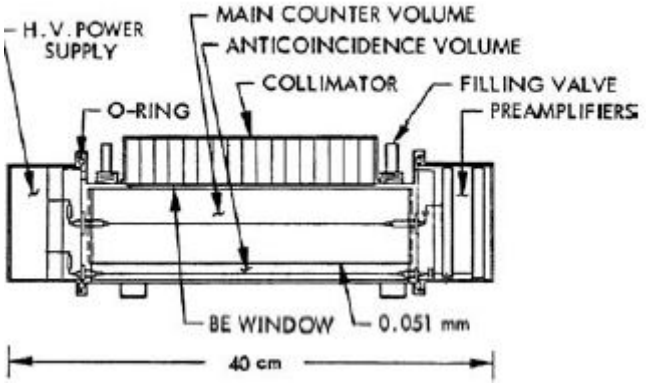

Figure 1.8: A schematic of proportional counter [Seward and Charles, 2010]

1.3.2 Gas-scintillation proportional counter (GSPC)

GSPCs are used to detect the scintillation or the optical flash that occurs when the ionized atoms in the gas recombine or rejoin with an electron. The only difference between the proportional counter and GSPC is that instead of the electron avalanche and charge collection section, we will have scintillation region and photo-multiplier tube (PMTs). A primary photoelectron is produced when an incident X-ray ionizes an atom in the detector gas volume. This photoelectron collides with other atoms, creating a secondary electron cloud which moves towards the bottom of the detector under the influence of the electric field. When the secondary electrons enter the high-field scintillation region, they gain enough energy to excite the gas atoms (usually xenon), which then form diatomic molecules through collisions. The molecules de-excite by the emission of UV photons, which pass through the exit window and are detected using PMTs. The relative amounts of light detected in each tube can be used to estimate the position of the incident X-ray. Its main advantage is that the variance of the scintillation step is less than that of the avalanche step. Hence, the minimum resolution achievable by a GSPC is approximately 7% at 6 keV, twice as good as a proportional counter. In recent years, GSPC is superseded by Charged couple devices (CCDs) for energies below 10 keV and CdZnTe (CZT) detectors for energies above 10 keV. European X-ray Observatory Satellite (EXOSAT), an European Space agency (ESA) satellite, consisted a Xe/He gas scintillation spectrometer (GSPC) in its instrumentation. Besides this, BeppoSAX contained High Pressure Gas Scintillation Proportional Counter (HPGSPC), which operates at high pressure (5 atmospheres).[Seward and Charles, 2010][arn, 2011]

1.3.3 The scintillation counters or Scintillators

Proportional counters cannot work efficiently at energies higher than 20 keV as the gas becomes transparent at higher energies. Therefore, we need a material with a high atomic number in this case. The scintillation counter uses the phosphor sandwich of NaI(Tl) on top of CsI(Na), where NaI crystal functions as the X-ray detector with the CsI used for background rejection. A phosphor sandwich or a "phoswich" detector is a combination of two different crystals. These crystals can efficiently stop photons with energies up to some MeV. The atoms in the crystals absorb incident photon's energy and translate some of this energy into scintillation. This scintillation is then detected by a PMT and registers the time of the event. Here, the amount of light in the scintillation is proportional to the energy of the incident X-ray photon. BeppoSAX contained Phoswich Detector System (PDS), which can absorb photons up to 300 keV.[Seward and Charles, 2010][arn, 2011]

1.3.4 Channel electron multiplier and Micro-channel plate (MCP)

The channel electron multiplier is a small diameter glass tube and has been treated to enhance secondary emission properties. The tube is maintained at high voltages. When a photon strikes the negative end of the tube or photocathode, it emits low energy electrons. The photocathode is generally coated with CsI. It helps in improving the efficiency of X-ray photoelectron emission. As these electrons accelerate down the tube towards the positive end, they strike the wall and liberate more electrons, which leads to a cascade of the electrons at the positive end (Figure 1.9).

MCP is a position-sensitive detector with high spatial resolution, and excellent quantum efficiency for low-energy X-rays and hence is the right choice of the detector for long-wavelength X-ray and extreme UV (EUV) spectroscopy with gratings. This instrument contains a plate composed of many small pores or tubes, side by side (Figure 1.9). Often they are inclined by an angle of a few degrees to the plate normal, so that incoming X-ray or UV photons strikes one side of a pore. In many designs, pairs of plates are used in series. The plates are imposed to high voltage electric field externally, so that when a photoelectron is produced by an X-ray impacting near the front surface of the plate, an avalanche occurs in the pore and a pulse of electrons comes out the positive end. These can be collected with anode wires, and their position determined with high accuracy, giving an imaging detector with good spatial resolution. MCPs are used in the Einstein and ROSAT high-resolution images (HRI) and the Chandra high-resolution camera (HRC).[arn, 2011]

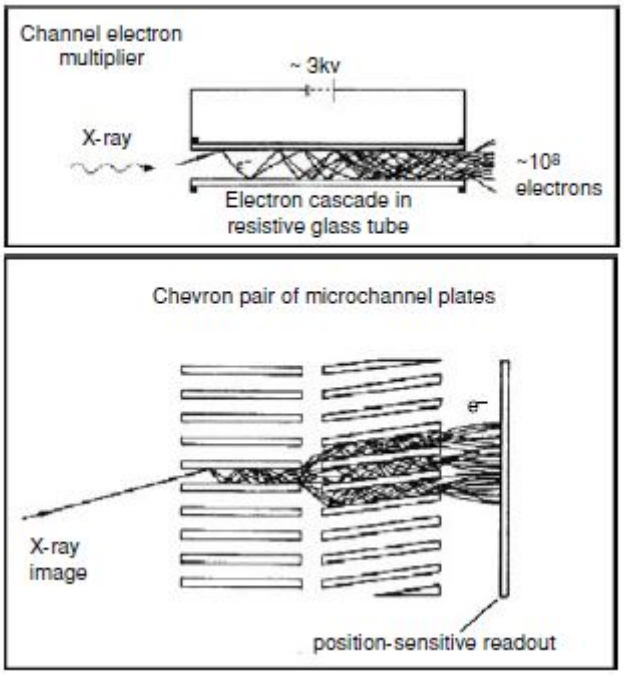

Figure 1.9: Channel electron multiplier and Micro-channel plate [Seward and Charles, 2010]

1.3.5 Charged Couple Devices (CCDs)

CCDs are semiconductor detectors with independent pixel readouts. In a CCD, the photons are incident on a silicon wafer where they create single or multiple electron-hole pairs. This charge is further amplified and read-out. The charges are captured in the depletion layer of the metal-oxide-semiconductor(MOS) capacitor. The gates are strategically placed very close to each other, and the charges are moved around by manipulating the voltages on the gates of the capacitors to allow the charge to spill from one capacitor to the next.[arn, 2011]

Readout scheme

The readout process could be very well explained with the help of an example of a bucket brigade. Suppose there is rainfall, and buckets are placed in a 2D array similar to pixels to capture the water droplets (photons). Suppose there is only one weighing scale to weigh the amount of water collected by a bucket. The columns of the buckets can be shifted down one by one After shifting one column, there is a conveyor belt at the end, which carries the buckets to the weighing scale individually and read the quantity of water (electrons generated). Similarly, all the intensity values are read by the CCD with the help of serial and parallel registers operating at different frequencies. Each pixel consists of 3 sub-pixels

(Metal-Oxide-Semiconductors). A Metal- Oxide- Semiconductor (MOS) capacitor has a potential difference between two metal plates separated by an insulator. The different potential is applied to different gates to move the charges. At the time t_1, the potential for phase one is high. So, there is a potential value created at the places where phase 1 is applied, and therefore, the electrons are present at only these places. At the next time instant, phase 1 and phase 2, both are turned high. Now, the potential well becomes broadened, and the electrons can move between the intermediate region. At the time, t_3, only phase 2 is high. So, the electrons are forced to move to the right. So, in this process, all the electrons have effectively shifted to a place, i.e., right to the first place. This process is repeated until the value of all the pixels has been read by the output amplifier.

Types of noises

There are different types of noises that are associated with CCDs at different level.
1. Read-Noise: This is the noise that occurs due to the different components involved in converting the photons to the final digital numbers that are stored in the computer.

$$S(DN) = PQE_i iS^v A_{CCD} A_1 A_2 \tag{1.20}$$

where $S(DN)$ represents the average signal for a group of pixels (DN), P is the average number of incident photons per pixel, QE_i is the interacting Quantum Efficiency (interacting photons/incident photons), i is the quantum yield (the number of electrons generated, collected and transferred per interacting photon), S^v is the sensitivity of the sense node; A_{CCD} is the output amplifier gain, A_1 is the gain of the signal processor, and A_2 is the gain of the ADC.

2. Shot noise: Consider light, a stream of discrete photons, is coming out of a laser pointer and hitting a wall to create a visible light spot. The fundamental physical processes that govern light emission are such that these photons are emitted from the laser at random times. However, the number of photons creating a light spot is so vast that the brightness, the number of photons per unit of time, varies only infinitesimally with time. However, if the laser brightness is reduced until only a handful of photons hit the wall every second, the relative fluctuations in the number of photons will be significant. These fluctuations are shot noise. Shot noise exists because phenomena such as light and electric current consist of the movement of discrete (also called "quantized") 'packets'.

3. Pixel non-uniformity noise: It arises due to different sensitivities in different pixels.

Pixel non-uniformity is a manifestation of processing variations and photo-mask alignment errors when the CCD is fabricated.

1.3.6 CZT detectors

CZT detectors or CdZnTe detectors are used for detecting X-rays at energies above 10 keV. It is a semiconductor and hence works the same as that of CCDs. The reason to use a CZT detector instead of a CCD at these energies is that CZT has a much higher cross-section than Si, so the detector has a better quantum efficiency. AstroSAT has CZT imager in its payload with energy range from 10-150 keV.

1.4 X-ray missions : The Neil Gehrels Swift Observatory

The Swift mission is a part of NASA's medium explorer (MIDEX) program and was launched into a low-Earth orbit on a Delta 7320 rocket on November 20, 2004. Dr. Brad Cenko, associated with NASA-GSFC, is the Principal investigator of this project. This project aimed to decipher the Gamma-ray mystery by observing the burst's afterglow. Some main mission objectives for Swift are to [Swi, a]

- Determine the origin of Gamma-ray bursts (GRBs).
- Classify GRBs and search for new types.
- Determine how the burst evolves and interacts with the surroundings.
- Use GRBs to study the early universe.
- Perform the first sensitive hard X-ray survey of the sky.

The payload of Swift comprised of three instruments: Burst Alert Telescope (BAT), X-ray telescope (XRT), UV/Optical Telescope (UVOT). Approximately 100 bursts are discovered by Swift each year. The Burst Alert Telescope (BAT) detects and positions the burst accurately. Within 20 seconds of the initial detection, Swift sends three arcminute position estimate of the burst to the ground. Immediately after the burst detection by BAT, the spacecraft point UVOT and XRT at the burst position.

1.4.1 Burst Alert Telescope (BAT)

Burst Alert Telescope (BAT) computes burst position onboard the satellite with arc-min positional accuracy. BAT has a large field of view (FOV) with 1.4 steradians (half-coded) and highly sensitive to an energy band of 15-150 keV. BAT is an excellent instrument to detect both weak and bright bursts. To detect weak bursts, it uses a two-dimensional coded aperture mask and a large area solid-state detector. BAT operates in two modes: burst mode and survey mode. Burst mode generates the position of the burst, whereas Survey mode generates hard X-ray survey data by collecting count-rate data for 80 energy intervals in five-minute time bins.

1.4.2 X-ray telescope (XRT)

It operates between the energy band 0.3-10 keV. XRT was built using the existing hardware form JET-X. It can take images that are used for higher accuracy position localization of the outburst and can obtain spectra of GRB afterglows. The light curves obtained are used to study flaring and the long-term decay of the X-ray afterglow.
The XRT can pinpoint a burst to 5 arcsec accuracy within 10 seconds of target acquisition and can study the X-ray counterparts of GRBs beginning 20-70 seconds from burst discovery and continuing for days to weeks [Swi, c].

Operation and control

It has different operating modes: Image Long and Short (IM), Windowed Timing (WT), Low rate (LR) and Piled-up Photo-Diode (PU), and Photon-Counting (PC) mode. For our purpose, we use WT and PC modes only.
WT mode has a time resolution of 1.7 ms and preserves 1D imaging. By 1D imaging, we mean that it preserves only the time information of the source.
PC mode obtain full spectral and spatial information of the source fluxes. The lower limit of the XRT sensitivity is $2X10^{-14}erg/cm^2/s$ in PC mode at 10^4 seconds.

1.4.3 UV/Optical Telescope (UVOT)

It operates between the wavelength band of 170-600 nm. It is a duplicate version of the XMM-Newton Optical Monitor (OM). Like XRT, it also takes images that are used for 0.5 arcsec position localizations and to study the temporal evolution of the UV/Optical afterglow. Moreover, it can also obtain spectra (via grism filter) of outbursts that are used to

determine the redshift via the observed wavelength of the Lyman-alpha cut-off [Swi, b].

X-ray transients

The celestial bodies are classified into Persistent or Transient sources based on the X-ray emission from them. Sources that continuously emit X-rays above the detectable range ($> 10^{32} ergs^{-1}$) are known as persistent sources. On the other hand, X-ray transients appear for a short period in the X-ray sky and then disappear. In other words, X-ray transient sources show, "Now you see me, and now you do not" behavior. Some of them reappear after a few weeks to a few years. X-rays are mainly produced from the accretion processes and accretion rate may varies with time. Therefore, the amount of X-rays produced by a given source varies with time. For example, Swift J1357.2-0933 is an X-ray transient. In general, X-ray transients have two states: a quiescent state and an outburst state. During the quiescent state, the X-ray emission from the source is undetectable. In other words, X-ray luminosity is less than $10^{32} ergs^{-1}$.Thus their observations require highly sensitive detectors. Many detections so far have been made with ROSAT, ASCA, and, more recently, with Chandra and XMM-Newton. In contrast, during an outburst, the source is very luminous in the X-ray regime. There are many X-ray transient sources discovered until now, like supernovae, novae, binary sources (Hard and Soft X-ray transients).

2.1 Why do we study X-ray transients

The reason behind the transient nature of a binary source is the tremendous amount of change in its accretion rate. Due to this, a sudden increase in the amount of luminosity is observed in these sources. The sudden increase in the X-ray luminosity above the detection limit is called an outburst. Therefore, X-ray transients are excellent sources to understand accretion processes, stellar structure, dynamics, and evolution. Moreover, discovery of new

transients in the X-ray sky allows us to perform population studies (see [Fabbiano, 2006] for more details). Some of the X-ray transients undergo large change in the X-ray luminosity, thus, luminosity dependence of the accretion geometry, and emission processes can be probed, e.g 4U 1630-47 [Kuulkers, 1998], [Tomsick et al., 2005].

2.2 Types of X-ray transients

As we discussed in the beginning of this chapter, X-ray transients experience sudden increase in mass accretion and then fade away after few weeks or months. The rise time in the luminosity curve or the period in which the peak X-ray luminosity reach is of the order of days, and the decay time of the burst is roughly about a few weeks to months. There are two types of X-ray transients based on their spectra - hard X-ray transients and soft X-ray transients. Hard X-ray transients are mostly observed in HMXBs with a compact object as a neutron star and the typical star, usually a Be star. On the other hand, the Soft X-ray transients (SXT) have a soft spectrum and associated with LMXBs. We will mainly focus SXTs in this chapter as the source under the study (Swift J1357.2-0933) belongs to LMXB class.

2.2.1 Soft X-ray transients (SXTs)

Soft X-ray transients (SXTs) are a subset of LMXBs that consist of either a weakly-magnetized neutron star or a black-hole as a compact object. Roughly one-fourth of the observed systems consist of neutron star as a compact object. SXTs are also known as X-ray novae (XRN). Most SXTs are in the quiescent state means they yield very weak X-ray fluxes and are optically faint (typically 20th magnitude or fainter) for most of the time. When the mass transfer onto the compact object becomes significant, a powerful X-ray outburst occurs. At this point, the accretion disc brightens dramatically, sometimes by as much as 7 or 8 magnitudes. SXTs containing black-hole and neutron star as compact objects have characteristic X-ray spectra, as shown in the Figure 2.1. As one can observe from Figure 2.1, both systems have the first component as a thermal accretion disc component, which dominates at low X-ray energies (soft energy band), but the second components in their spectra are different [Seward and Charles, 2010]:

- As shown in the spectrum of Nova Mus 1991 (left panel of the 2.1), the black-hole SXTs commonly exhibit a power-law component, which can extend to extremely

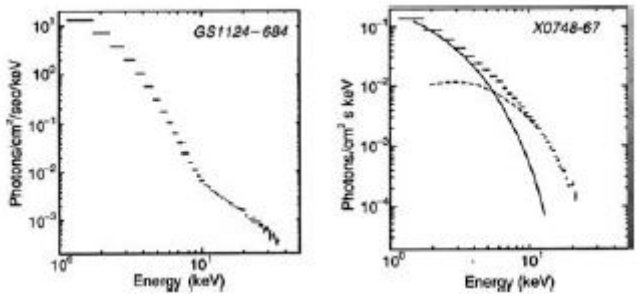

Figure 2.1: The figure shows the spectrum of the black-hole candidate (BHC) Nova Mus 1991 (left panel) and the X-ray burster X0748-676 (right panel). The BHC spectrum is dominated at low energies by a thermal component but has an underlying hard power-law component that extends to very high energies. The X-ray burster, on the other hand, has two thermal components, one from the disc, the other from the neutron star [Seward and Charles, 2010].

high energies (hard spectra is detected in this object up to several hundred keV [Sunyaev et al., 1992]).

- The right panel of the 2.1 shows the neutron star SXT system in which the second component is also a thermal component, but this one is harder (or hotter) than that of the disk. This additional thermal component is well-fit by a single temperature blackbody, which gives a strong clue as to its likely origin, namely, the surface of the neutron star itself. It is here that the accreted material comes to rest and stores its kinetic energy.

There are some spectral states when no disc emission is observed in a black hole system. For example, [Done et al., 2013] used an alternate way to constrain the black-hole spin in a subclass of narrow-line Seyfert 1 (NLS1) active galactic nuclei as the disc peaks at energies just below the soft X-ray bandpass. However, there are studies which have shown that there are similarities in neutron star and black-hole (see [van der Klis, 1994] for details). SXTs can be well-explained by Disk Instability Model (DIM).

2.2.2 Disk Instability Model

According to this model, an accretion disk has two states: a cold neutral state and a hot fully-ionized state. The cold state is the quiescent state. In this state, the viscosity of the matter is too small to allow a stable accretion flow. As matter from the donor star accumulates in the outer disk, the surface density, and temperature of the disk gradually increase. When the surface density becomes equal to a particular critical value, the disk jumps to the hot spot

because of thermal instability. This state triggers as accreted mass flows into the inner part of the disk, which causes an X-ray outburst. When the surface density drops below another critical value, the disk returns to the quiescent state.[Joachim E Trümper, 2008]

2.3 Classification of X-ray transients

Wijnands et al. classified X-ray transients [Wijnands et al., 2006] into three classes based on their peak X-ray luminosity, that are:

- **Bright to very bright X-ray transients**: The peak X-ray luminosity of these transients lie between $10^{37} - 10^{39} ergs^{-1}$.
- **Faint X-ray transients**: The peak X-ray luminosity of these transients lie between $10^{36} - 10^{37} ergs^{-1}$.
- **Very faint X-ray transients (VFXTs)**: The peak X-ray luminosity of these transients lie between $10^{34} - 10^{36} ergs^{-1}$.

2.4 Very faint X-ray transients (VFXTs)

Very faint X-ray transients have the least X-ray luminosity among all the X-ray transient classes. We know very little about them. The reason simply is the faintness and the shortness of their outbursts. Thus, it is tough to catch these outbursts. These faint outbursts are believed to occur due to radiatively inefficient accretion of mass onto the compact object. These VFXTs are likely accreting neutron star, and black-hole.

X-ray data alone is insufficient to ascertain the exact nature of these systems and, therefore, we need multi-wavelength (IR/optical) observations to know the exact nature of the source.[Wijnands et al., 2015] Moreover, VFXTs do not show the spectral properties as other classes of transients (see [Heinke et al., 2015] for more details). Therefore, their timing analysis cannot be done. So, we need other alternatives to do their study. We will discuss the analysis of one such source in next chapter in detail. To detect VFXTs, we need detectors with:

- High sensitivity
- Large Field of View (FOV)
- Rapid data turn around time

- (sub)arcsecond resolution

Swift J1357.2-0933

In the last chapter, we discussed X-ray transients and their classes. The source that we study belongs to Very faint X-ray transients (VFXTs), and it is named as Swift J1357.2-0933. The most beautiful thing about this source is this is the only "confirmed" black-hole belonging to VFXT. It is a LMXB X-ray transient with galactic coordinates l = $328^{\circ}.702$, and b = $+50^{\circ}.004$ [Krimm et al., 2013]. Swift J1357.2-0933 has undergone three outbursts in the last eight years, which lasted for a few months, unlike the majority of VFXTs. The first-ever outburst in this source was observed in May 2011 [Armas Padilla et al., 2012]. This outburst lasted for nearly three months. The second outburst of this source is observed after six years in 2017 [Beri et al., 2019], and the recent outburst one in 2019. The detection of optical dips both in outburst [Corral-Santana et al., 2013] and quiescence [Shahbaz et al., 2013] suggest that this source is highly inclined. From its radial velocity profile, the source is known to have a 2.8-hour orbital period and mass function $f(M_1) > 3.0M_{\odot}$ at a 95.4% confidence level [Corral-Santana et al., 2013]. These results strongly imply that the source is a black-hole. The binary mass function can be determined by equation (1.3). By putting all the relevant values for the source in equation (1.3), it turns out that the system consists of a black-hole of mass greater than $9.3M_{\odot}$ and an $\sim$ M2V companion star of mass $\sim 0.4M_{\odot}$ [Mata Sánchez et al., 2015].

[Wijnands et al., 2015] compared several neutron star systems with black-hole systems, and found that most black-hole binaries have significantly harder spectra at luminosities of $10^{34} - 10^{35} ergs^{-1}$ (see left plot of Figure 3.1). Black points of right plot of Figure 3.1 refer to black-hole candidates while grey points represent neutron stars. It was found that X-ray

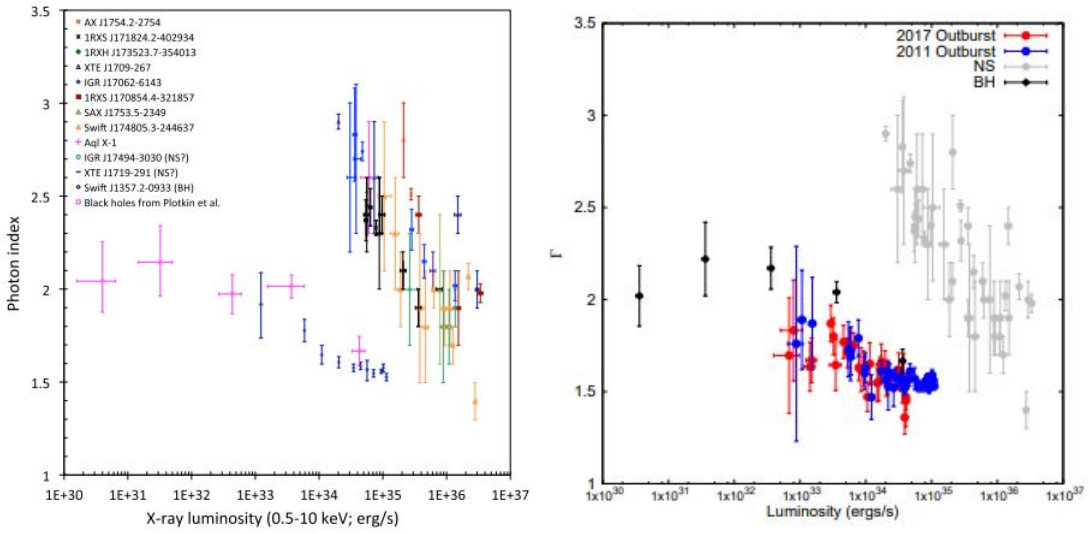

Figure 3.1: Both of the plots are showing trend followed by NS and BH systems. The plot on the left is taken from [Wijnands et al., 2015] and the plot on the right is taken from [Beri et al., 2019].

data of Swift J1357.2-0933 during its 2011 and 2017 outbursts followed the track of black-holes (see [Beri et al., 2019] for more details). Thus, this was another fact that supported nature of the accretor to be a black-hole.

There have been several claims of distance to the source. [A. Rau, 2011] identified donor to be quiescent star at a distance of 1.5 kpc. Recently, [Russell et al., 2018] studied 6 year optical/infrared light curve of Swift J1357.2-0933 during quiescence and found that their results do not support distance estimates of 1.5 kpc but the possible distance range out to 6 kpc. For the analysis of 2019 outburst, we assumed the distance to be 1.5 kpc as assumed for 2011 and 2017 outbursts of the source. Swift multiwavelength observatory has observed all the three outburst of the source and provided astronomers with XRT and UVOT data. In this chapter, we discuss the softwares we used to analyze the data of the 2019 outburst of Swift J1357.2-0933, and the results that we get.

3.1 Analysis of 2019 outburst

The data for 2019 outburst of Swift J1357.2-0933 was proposed by Project Investigator (PI) Dr. Aru Beri, and the analysis is carried out by us. We have carried out data analysis with the NASA's software package "HEASoft" that contains tools known as FTOOLS to

process source data. In this section, we discuss FTOOLS we use in the analysis of Swift J1357.2-0933.

3.1.1 HEASARC

HEASARC is NASA's repository for X-ray, gamma-ray, and cosmic microwave background data. It is a collaboration between the Goddard Space Flight Center (GSFC) and the Harvard-Smithsonian Center for Astrophysics (CIA). It provides access to public data for all currently operating X-ray missions and all major past missions (both US and non-US missions) [arn, 2011].

3.1.2 FTOOLS

- **Xselect**[1]: This command-line program systematized the input of data through the observation catalog, and store it for further use. It can hold information on many instruments using a mission database file and used to make appropriate calibration products. It applies selection criteria to the Housekeeping and auxiliary filter data and makes good time intervals (GTI). It is also used to extract images, spectra, and light curves from the event data by using the entered filters and the GTI created by the applied selections.

- **DS9**[2]: SAOImage DS9 is a tool for data visualization and astronomical imaging. It supports FITS images and binary tables, multiple frame buffers, region manipulation, and many scale algorithms and colormaps. It also helps in providing accessible communication with external analysis tasks. Besides this, it also supports advanced features such as 2-D, 3-D, and red-green-blue (RGB) frame buffers, and many features of imaging like scaling, arbitrary zoom, cropping, rotation, and a variety of coordinate systems.

- **XIMAGE**[3]: It is a command-line tool that displays and analyze multi-mission X-ray image. It is designed such that if the proper calibration files are available, it can support the data analysis from any X-ray imaging detector. Besides, it also supports some fundamental analysis of radio, optical, and infrared images. The display and graphic capabilities of XIMAGE are based on the PGPLOT graphic package. Besides PGPLOT, programs like SAOImage and POWplot is also generated to display images

[1] https://heasarc.gsfc.nasa.gov/docs/software/lheasoft/ftools/xselect/node2.html
[2] http://ds9.si.edu/site/Home.html
[3] https://heasarc.gsfc.nasa.gov/docs/xanadu/ximage/manual/ximage.html

and select regions. Some functions of XIMAGE are mission independent e.g., display while others are not e.g., source detect. XIMAGE can read in the images from the unknown mission, but to get detailed analysis, the user should provide it with the mission name. One can give the command chmdb/list to obtain the list of known missions.

- **XSPEC**[4]: It is an X-ray spectral fitting program that is entirely detector-independent and thus can be used for any spectrometer. The observed spectrum is related to the actual spectrum of the source ($f(E)$) by:

$$C(I) = \int f(E)R(I,E)dE \tag{3.1}$$

Where $C(I)$ is the photon count within specific instrument channels, $R(I,E)$ is the instrumental response. It is proportional to the probability that an incoming photon of energy E will be detected in channel I. Then one can determine the actual spectrum of a source, $f(E)$, by inverting this equation, thus can derive $f(E)$ for a given set of $C(I)$. Unfortunately, such inversions tend to be non-unique and unstable to small changes in $C(I)$. Thus, the conventional alternative is to choose a model spectrum, $f(E)$ with some parameters $f(E, p1, p2, ...)$, and fit it to the data generated by the spectrometer. For every $f(E)$, a predicted count spectrum ($C_p(I)$) is calculated and compared to the observed data ($C(I)$). Then, a "fit statistic" is computed from this comparison and used to decide whether the model spectrum "fits" the data or not. Then, the model parameters are varied to find the parameter values that give the most desirable fit statistic. These values are called the best-fit parameters. The model spectrum, $f_b(E)$, made up of the best-fit parameters is considered to be the best-fit model.

The statistic we used in this thesis work is Cash-statistic or C-statistic. We use C-statistic instead of more commonly used χ^2-statistic because it has been shown that for the analysis of X-ray spectra, C-statistic provides unbiased estimates of the model parameters and their uncertainty ranges when applied to bins with a small number of counts. Not only that, it is also proven that the C-statistic can also be used for statistical tests such as assessing the goodness of fit of a spectral model. C-statistic is given as [Kaastra, 2017]:

[4]https://heasarc.gsfc.nasa.gov/xanadu/xspec/manual/XspecManual.html

$$\tilde{C} = 2\Sigma_{i=1}^{n} s_i - N_i ln(s_i) \tag{3.2}$$

where N_i is the observed number of counts and s_i is the expected number of counts for the tested model.

3.1.3 Spectral fitting models

There are plenty of models that can be used for X-ray spectral fitting in XSPEC. The model fitting is beneficial as it provides us with the source information and the environment surrounding the source. In the spectral analysis of Swift J1357.2-0933, we use following models:

- **tbabs**[5]: The Tuebingen-Boulder ISM absorption or tbabs model is a multiplicative model, used to calculate the cross-section for X-ray absorption by the Interstellar medium (ISM) by summing up the cross-sections for X-ray absorption due to the different phases of ISM. These phases are the gas-phase ISM, the grain-phase ISM, and the molecules in the ISM. The cross-section of X-ray absorption in the gas-phase ISM is the sum of the cross-sections of the photoionization of different elements that are weighted by abundance, and takes into account the depletion onto grains. We set the abundance through *abund wilm* command in the XSPEC. The grain-phase ISM accounts for the effect of shielding by the grains and is extremely small. The molecular contribution to the ISM cross-section only accounts for the molecular hydrogen. There is only one variable parameter in this model and that is equivalent hydrogen column (N_H) in units of 10^{22} atoms cm^{-2}.

- **po**[6]: This is an additive simple photon power law model given as :

$$A(E) = KE^{-\alpha} \tag{3.3}$$

where there are two variable parameters: dimensionless α (photon index of power law), and K (norm in photons/keV/cm^2/s at 1 keV).

- **cflux**[7]: The calculate flux or cflux is a convolution model used to calculate the flux of other model components. For example, in our study, we use cflux*tbabs*po model

[5]https://heasarc.gsfc.nasa.gov/xanadu/xspec/manual/node265.html
[6]https://heasarc.gsfc.nasa.gov/xanadu/xspec/manual/node213.html
[7]https://heasarc.gsfc.nasa.gov/xanadu/xspec/manual/node280.html

to calculate flux. There are three variable parameters in this model: E_{min}, E_{max} (minimum and maximum energy over which the flux is calculated), and log_{10} flux (in erg/cm^2/s).

3.1.4 X-ray spectral analysis

The data collected by the satellite is raw. It contains noise and signals from background sources. There are different levels at which this raw data is processed into a "clean event" file, which is used for further analysis. The raw data undergoes a small amount of processing and gets converted into a Level 1 FITS file. To create a Level 2 calibrated or "clean" event file, Level 1 event files and image files undergo the data screening and coordinate transformation [8].

We start the X-ray spectral analysis by generating Level 2 clean event files via running xrtpipeline command in HEASoft. We extract images from these files by loading them in XIMAGE. Then we extract the background and source region from these images using the Xselect tool. For PC mode, we take 50 pixels (118 arcsec) region, and for WT mode, we take 20 pixels (47.2 arcsec) region. Then we filter out these regions and extract the background and source spectrum. For the extraction of the spectrums, we use arf (ancillary response files) and corresponding rmf (response matrices) files, which we get from "Built XRT products" and load rmf, arf, background spectrum and source spectrum in XSPEC. The spectrums that we get after doing all this are raw spectrums which contain both good and bad channels. By bad channels, we mean to say the channels which do not have any signal. Thus, we binned the spectrums using GRPPHA and set the minimum bin such that we get one photon count per channel as the source we are studying is "Very faint" in the X-ray sky. For this purpose, we use Cash statistics. We ignore bad channels and convert the channel-axis to the energy-axis in the spectrums. We then choose an energy range corresponding to Windowed Timing (WT) (0.7-10 keV) and Photon Count (PC) mode (0.3-10 keV). We are reporting our results in this thesis in the one-sigma confidence range. We fit the spectrum using absorption model with simple power-law (tbabs*po) model with energy range 0.5-10 keV and neutral hydrogen number density (N_H) as 0.012 atoms cm^{-2}. We use cflux*tbabs*po model for flux calculation and setting N_H to 0.

[8] https://www.swift.ac.uk/analysis/xrt/files.php

3.1.5 UV/Optical spectral analysis

We loaded the properly caliberated files (filename.sk.img) into the DS9 tool for source and background region extraction. We take 5 arcsec for source region and 20 arcsec for background region extraction. Then, we ran uvotproduct command in HEASoft. We included timezero = TSTART+TELAPSE and combined the observations to provide a minimum detection level of 3 sigma by including $rebin = MIN\_SIGMA = 3$ in the command-line. We loaded caliberated files as input files, extracted region files, and obtain FITS file for each observation. Using these FITS files, we noted down the magnitude and UVOT flux values. We have corrected the magnitudes and fluxes for the Galactic extinction. The reddening E(B-V) is 0.04 mag in the direction of J1357. We have used the following A_λ values of extinction: A_V = 0.123, A_B = 0.163, A_U = 0.193, A_{UVW1} = 0.263, A_{UVM2} = 0.387, A_{UVW2} = 0.349, which were obtained by [Armas Padilla et al., 2012]. For the extinction correction in magnitude values, we subtract the above extinction values from the observed magnitude of each observation for each filter. For extinction correction in flux values, we multiply the flux values with (A_λ/ reddening factor) for each filter. To obtain Figure 3.4, we plotted the XRT flux values corresponding to the UVOT flux values for each observation.

3.1.6 Results

X-ray spectral analysis results

The results of X-ray spectral analysis of 2019 outburst of Swift J1357.2-0933 are shown in Table 1. The highlighted values in the table show the peak X-ray luminosity of 2019 outburst which is coming out to be $\sim 1.60 \pm 0.27 \times 10^{33} ergs^{-1}$ and minimum X-ray luminosity is $\sim 0.13 \pm 0.05 \times 10^{33} ergs^{-1}$. Figure 3.2 is the count-rate plot, which shows that during the outburst, the photon counts/sec is maximum, and its decline with the decay of the outburst. However, the count rate is very low, i.e., 3.16×10^{-1} counts/sec, which implies that the outburst is very faint. Figure 3.3 is the two-panel plot. The upper panel shows that the luminosity follows the same trend as the count-rate plot. The lower panel represents the curve of Photon-index Vs. Time. As we can observe from this plot, the photon-index is maximum, which means that the hardness ratio is lower at the peak of the outburst. Hardness ratio is the ratio of the photons in hard energy band to the photons in the soft energy band. In XRT, 0.5-2 keV is considered a soft energy band and 2-10 keV as a hard energy band.

Table 1: Log of Swift observations and XRT spectral results of 2019 outburst

Obs ID	Time(MJD)	Mode	Exp.time(ksec)	Γ	$F^a_{X,unabs}$	L^b_X	$red\chi^2_\nu(dof)$
31918084	58630.2533	WT	1.31	$3.58^{+0.65}_{-0.70}$	$5.95^{+1.02}_{-1.04}$	$1.60^{+0.27}_{-0.28}$	0.62 (64)
31918085	58632.2957	WT	1.51	$2.28^{+0.23}_{-0.22}$	$4.17^{+0.43}_{-0.42}$	$1.12^{+0.13}_{-0.11}$	0.73 (153)
88872001	58633.0559	PC	1.10	1.68 ± 0.11	$6.02^{+0.44}_{-0.47}$	$1.62^{+0.13}_{-0.12}$	0.74 (132)
31918086	58636.5232	PC	1.58	1.66 ± 0.09	$5.45^{+0.37}_{-0.37}$	$1.47^{+0.1}_{-0.09}$	0.83 (164)
31918087	58642.2938	PC	1.59	1.76 ± 0.10	$4.53^{+0.32}_{-0.34}$	$1.22^{+0.09}_{-0.08}$	0.71 (142)
31918088	58649.1678	PC	1.42	1.56 ± 0.12	$4.88^{+0.44}_{-0.41}$	$1.31^{+0.13}_{-0.11}$	1.09 (108)
31918089	58654.1139	PC	1.22	1.83 ± 0.13	$3.67^{+0.34}_{-0.32}$	$0.99^{+0.09}_{-0.08}$	0.94 (98)
31918090	58660.1249	PC	1.63	1.93 ± 0.12	$3.01^{+0.26}_{-0.24}$	$0.81^{+0.07}_{-0.06}$	0.89 (113)
31918091	58662.6706	PC	0.67	1.50 ± 0.25	$3.85^{+0.58}_{-0.53}$	$1.04^{+0.16}_{-0.14}$	0.76 (43)
31918092	58668.5556	PC	0.54	$2.44^{+0.36}_{-0.34}$	$1.19^{+0.26}_{-0.22}$	$0.32^{+0.07}_{-0.06}$	0.82 (24)
31918093	58672.5342	PC	0.99	1.42 ± 0.16	$4.49^{+0.52}_{-0.49}$	$1.21^{+0.14}_{-0.13}$	0.55 (70)
31918094	58682.1041	PC	1.39	2.12 ± 0.17	$1.78^{+0.21}_{-0.19}$	$0.48^{+0.06}_{-0.05}$	0.61 (70)
31918095	58692.9878	PC	1.34	$1.23^{+0.60}_{-0.59}$	$0.32^{+0.14}_{-0.11}$	$0.09^{+0.03}_{-0.04}$	0.91 (7)
31918096	58703.8096	PC	1.49	$1.63^{+0.58}_{-0.55}$	$0.49^{+0.19}_{-0.15}$	$0.13^{+0.05}_{-0.04}$	0.81 (9)

Flux in the units of $10^{-12}\ erg\ cm^{-2}\ s^{-1}$ in the 0.5-10 keV energy band.
X-ray luminosity in units of $10^{33}\ erg\ s^{-1}$ calculated from the 0.5-10 keV unabsorbed flux by taking distance as 1.5 kpc.

UV/Optical spectral analysis

From UVOT analysis, the corrected magnitude value corresponding to the outburst peak in different filters are found out to be 15.28 ± 0.34 in UVM2 filter with corresponding flux value of $2.43 \pm 0.11 \times 10^{-14}$, and 15.40 ± 0.22 in UVW1 filter with corresponding flux value of $1.42 \pm 0.05 \times 10^{-14}$ (Figure 3.3). The minimum corrected magnitude value towards the decay of the outburst is found out to be 20.112 ± 0.50 (Figure 3.4).

3.1.7 Discussion

We compare the results of 2019 outburst with 2011 and 2017 outbursts of Swift J1357.2-0933. On comparing the X-ray spectral data of these outbursts, it turns out that the peak X-ray luminosity of 2019 outburst is roughly order of 10 lower than 2017 outburst and roughly order of 100 lower than 2011 outburst, which implies that 2019 outburst is the faintest burst observed in this object until now. On comparing the count rate plots of the three outbursts, it turns out that the count rate is roughly an order of 100 lower than the 2017 outburst. Thus, there is also this possibility that we may have missed the peak of the outburst. Moreover, the Photon-index plot of 2019 shows a different trend comparing to

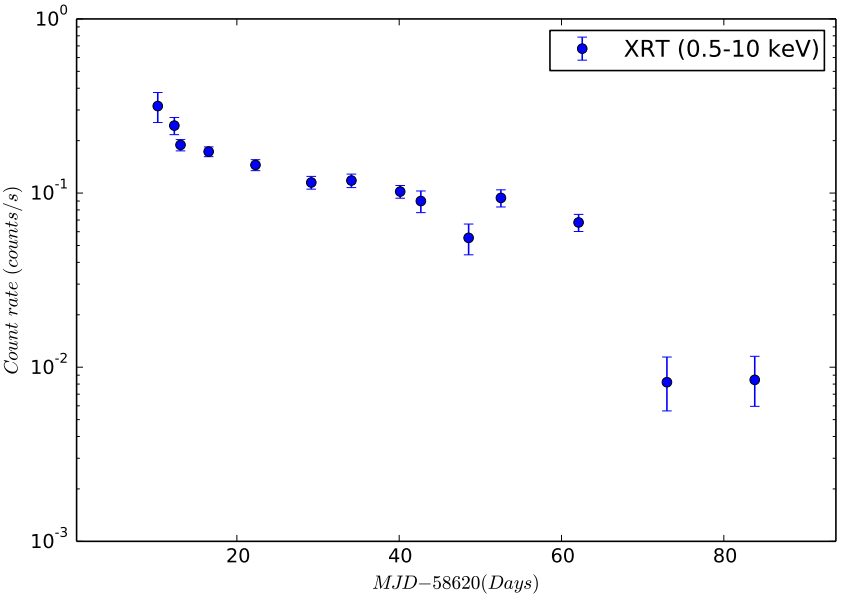

Figure 3.2: The above plot shows the count rate curve during the 2019 outburst of Swift J1357.2-0933. The X-axis shows the time of observation. The Y-axis represents count rate in the unit of counts s^{-1}. The Y-axis is plotted in log scale.

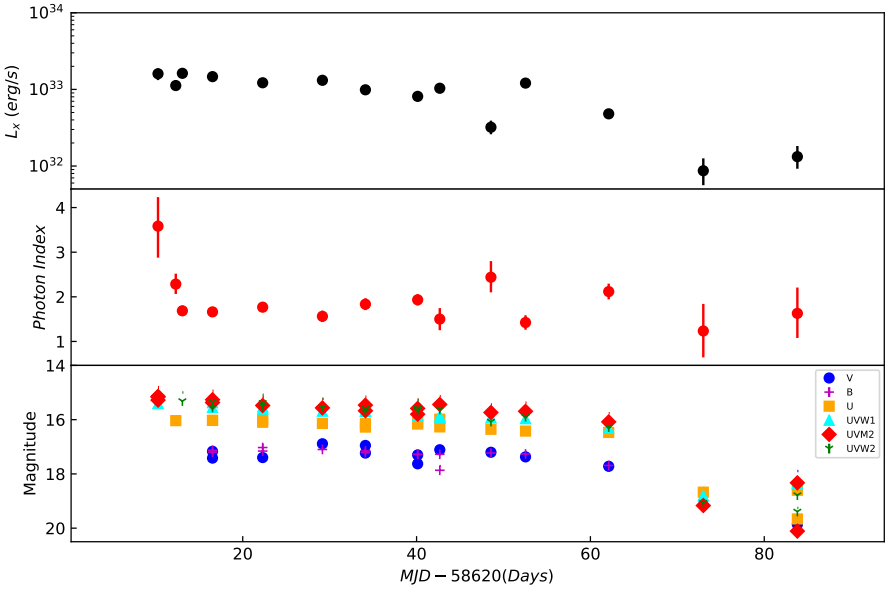

Figure 3.3: The upper panel is the light curve in the 0.5–10 keV band obtained using the Swift-XRT observations of 2019 outburst of Swift J1357.2-0933 (by taking source distance = 1.5 kpc), the middle panel is the photon index (Γ) evolution with time while in the bottom panel represents the UV/optical light curves in the Vega system.

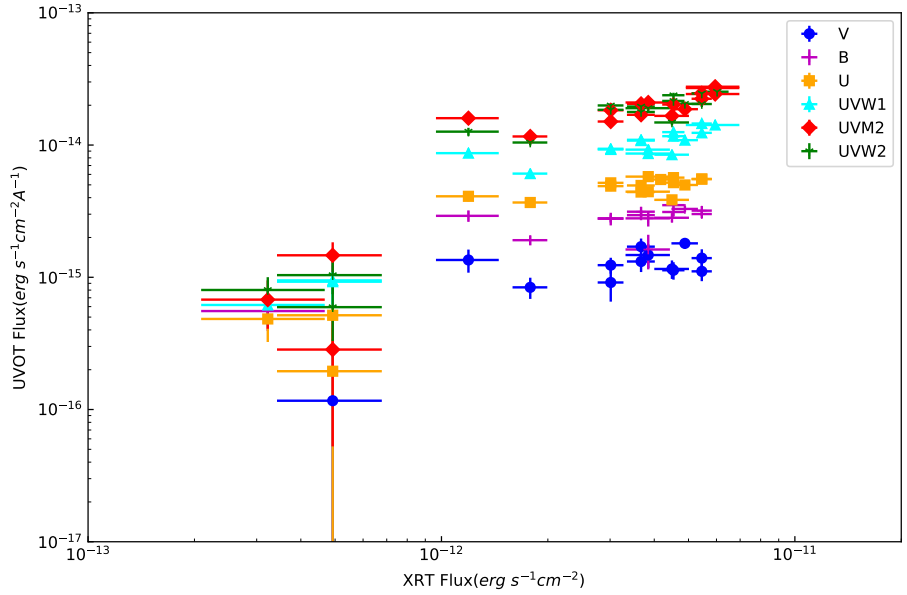

Figure 3.4: The Y-axis represents the UVOT flux corresponding to the XRT flux during the outburst of the source. Both axis are plotted in logscale.

the previous outbursts. We need to do the detailed timing analysis of the object, which is possible by using NICER data, which is our next objective.

From Figure3.3, we observed that close to end of the 2019 outburst of Swift J1357.2-0933 optical/UV magnitudes were as low as 20. while during its previous outbursts the lowest value recorded was 17. We also found a clear correlation between optical/UV and X-ray flux which is similar to that observed during its previous outbursts ([Armas Padilla et al., 2012] and [Beri et al., 2019]). However, the values of optical/UV fluxes were orders of magnitude compared to that observed during its 2011 and 2017 outburst, indicating that the 2019 outburst was fainter in optical/UV as well.

3.1.8 Future plans

Several black hole low mass X-ray binaries have displayed the decay profiles which are well modeled/explained by disc-instability model including irradiation of the accretion disc. During the 2017 outburst of Swift J1357.2-0933, [Beri et al., 2019] performed a detailed study of correlation between optical/UV and X-ray flux to understand the origin of optical/UV emission in this source and found that viscously heated disc well explained the optical emission while proposed that plausible cause for the UV emission could be X-ray reprocessing. In future, we aim to perform a similar analysis as done in [Beri et al., 2019]

to investigate the origin of optical/UV emission during the 2019 outburst of Swift J1357.2-0933.

Bibliography

[Swi, a] The neil gehrels swift observatory. https://www.swift.ac.uk/about/index.php.

[Swi, b] Swift uvot data analysis. https://www.swift.ac.uk/analysis/uvot/.

[Swi, c] The swift xrt data reduction guide. https://swift.gsfc.nasa.gov/analysis/xrt_swguide_v1_2.pdf.

[arn, 2011] (2011). *Handbook of X-ray Astronomy*. Cambridge Observing Handbooks for Research Astronomers. Cambridge University Press.

[A. Rau, 2011] A. Rau, J. Greiner, R. F. (2011). 3140:1.

[Armas Padilla et al., 2012] Armas Padilla, M., Degenaar, N., Russell, D. M., and Wijnands, R. (2012). Multiwavelength spectral evolution during the 2011 outburst of the very faint x-ray transient swift j1357.20933. *Monthly Notices of the Royal Astronomical Society*, 428(4):3083–3088.

[Beri et al., 2019] Beri, A., Tetarenko, B. E., Bahramian, A., Altamirano, D., Gandhi, P., Sivakoff, G. R., Degenaar, N., Middleton, M. J., Wijnands, R., Hernández Santisteban, J. V., and et al. (2019). The black hole x-ray transient swift j1357.2–0933 as seen with swift and nustar during its 2017 outburst. *Monthly Notices of the Royal Astronomical Society*, 485(3):3064–3075.

[Corral-Santana et al., 2013] Corral-Santana, J. M., Casares, J., Munoz-Darias, T., Rodriguez-Gil, P., Shahbaz, T., Torres, M. A. P., Zurita, C., and Tyndall, A. A. (2013). A black hole nova obscured by an inner disk torus. *Science*, 339(6123):1048–1051.

[Done et al., 2013] Done, C., Jin, C., Middleton, M., and Ward, M. (2013). A new way to measure supermassive black hole spin in accretion disc-dominated active galaxies. *Monthly Notices of the Royal Astronomical Society*, 434(3):1955–1963.

[Eggleton, 1983] Eggleton, P. P. (1983). Aproximations to the radii of Roche lobes. *ApJ*, 268:368–369.

[Fabbiano, 2006] Fabbiano, G. (2006). Populations of x-ray sources in galaxies. *Annual Review of Astronomy and Astrophysics*, 44(1):323–366.

[Frank et al., 2002] Frank, J., King, A., and Raine, D. (2002). *Accretion Power in Astrophysics*. Cambridge University Press, 3 edition.

[Heinke et al., 2015] Heinke, C. O., Bahramian, A., Degenaar, N., and Wijnands, R. (2015). The nature of very faint x-ray binaries: hints from light curves. *Monthly Notices of the Royal Astronomical Society*, 447(4):3034–3043.

[Joachim E Trümper, 2008] Joachim E Trümper, G. H. (2008). *Universe in X-rays*. Springer, Berlin, Heidelberg, 1 edition.

[Kaastra, 2017] Kaastra, J. S. (2017). On the use of C-stat in testing models for X-ray spectra. *A&A*, 605:A51.

[Krimm et al., 2013] Krimm, H. A., Holland, S. T., Corbet, R. H. D., Pearlman, A. B., Romano, P., Kennea, J. A., Bloom, J. S., Barthelmy, S. D., Baumgartner, W. H., Cummings, J. R., Gehrels, N., Lien, A. Y., Markwardt, C. B., Palmer, D. M., Sakamoto, T., Stamatikos, M., and Ukwatta, T. N. (2013). THE SWIFT /BAT HARD x-RAY TRANSIENT MONITOR. *The Astrophysical Journal Supplement Series*, 209(1):14.

[Kuulkers, 1998] Kuulkers, E. (1998). Towards 4u163047: a black-hole soft x-ray transient odyssey. *New Astronomy Reviews*, 42(9-10):613–616.

[Mata Sánchez et al., 2015] Mata Sánchez, D., Muñoz-Darias, T., Casares, J., Corral-Santana, J., and Shahbaz, T. (2015). Swift J1357.2−0933: a massive black hole in the Galactic thick disc. *Mon. Not. Roy. Astron. Soc.*, 454(2):2199–2204.

[M.C.Ramadevi,] M.C.Ramadevi. X-ray binaries. `http://www.iucaa.in/~dipankar/ph217/contrib/xrb.pdf`.

[Russell et al., 2018] Russell, D. M., Qasim, A. A., Bernardini, F., Plotkin, R. M., Lewis, F., Koljonen, K. I. I., and Yang, Y.-J. (2018). Optical precursors to black hole x-ray

binary outbursts: An evolving synchrotron jet spectrum in swift j1357.2–0933. *The Astrophysical Journal*, 852(2):90.

[Seward and Charles, 2010] Seward, F. D. and Charles, P. A. (2010). *Exploring the X-ray Universe*. Cambridge University Press, 2 edition.

[Shahbaz et al., 2013] Shahbaz, T., Russell, D. M., Zurita, C., Casares, J., Corral-Santana, J. M., Dhillon, V. S., and Marsh, T. R. (2013). Evidence for quiescent synchrotron emission in the black hole X-ray transient Swift J1357.2-0933. *MNRAS*, 434(3):2696–2706.

[Shao and Li, 2015] Shao, Y. and Li, X.-D. (2015). Formation and evolution of galactic intermediate/low-mass x-ray binaries. *The Astrophysical Journal*, 809(1):99.

[Sunyaev et al., 1992] Sunyaev, R., Churazov, E., Gilfanov, M., Dyachkov, A., Khavenson, N., Grebenev, S., Kremnev, R., Sukhanov, K., Goldwurm, A., Ballet, J., Cordier, B., Paul, J., Denis, M., Vedrenne, G., Niel, M., and Jourdain, E. (1992). X-Ray Nova in Musca (GRS 1124-68): Hard X-Ray Source with Narrow Annihilation Line. *ApJL*, 389:L75.

[Tauris and van den Heuvel, 2003] Tauris, T. M. and van den Heuvel, E. (2003). Formation and evolution of compact stellar x-ray sources.

[Tomsick et al., 2005] Tomsick, J. A., Corbel, S., Goldwurm, A., and Kaaret, P. (2005). X-ray observations of the black hole transient 4u 1630-47 during 2 years of x-ray activity. *The Astrophysical Journal*, 630(1):413–429.

[van der Klis, 1994] van der Klis, M. (1994). Similarities in Neutron Star and Black Hole Accretion. *ApJS*, 92:511.

[Wijnands et al., 2015] Wijnands, R., Degenaar, N., Armas Padilla, M., Altamirano, D., Cavecchi, Y., Linares, M., Bahramian, A., and Heinke, C. O. (2015). Low-level accretion in neutron star x-ray binaries. *Monthly Notices of the Royal Astronomical Society*, 454(2):1371–1386.

[Wijnands et al., 2006] Wijnands, R., in't Zand, J. J. M., Rupen, M., Maccarone, T., Homan, J., Cornelisse, R., Fender, R., Grindlay, J., van der Klis, M., Kuulkers, E., Markwardt, C. B., Miller-Jones, J. C. A., and Wang, Q. D. (2006). The XMM-Newton/Chandra monitoring campaign of the Galactic center region. Description of the program and preliminary results. *A&A*, 449(3):1117–1127.